

## 2 In-situ calibration of the single-photoelectron charge 3 response of the IceCube photomultipliers

---



4 ICECUBE

### 5 IceCube collaboration

6 M. G. Aartsen,<sup>p</sup> M. Ackermann,<sup>bc</sup> J. Adams,<sup>p</sup> J. A. Aguilar,<sup>l</sup> M. Ahlers,<sup>t</sup> M. Ahrens,<sup>at</sup>  
7 C. Alispach,<sup>z</sup> K. Andeen,<sup>ak</sup> T. Anderson,<sup>az</sup> I. Ansseau,<sup>l</sup> G. Anton,<sup>x</sup> C. Argüelles,<sup>n</sup>  
8 J. Auffenberg,<sup>a</sup> S. Axani,<sup>n</sup> P. Backes,<sup>a</sup> H. Bagherpour,<sup>p</sup> X. Bai,<sup>aq</sup> A. Balagopal V.,<sup>ac</sup>  
9 A. Barbano,<sup>z</sup> S. W. Barwick,<sup>ab</sup> B. Bastian,<sup>bc</sup> V. Baum,<sup>aj</sup> S. Baur,<sup>l</sup> R. Bay,<sup>h</sup> J. J. Beatty,<sup>r,s</sup>  
10 K.-H. Becker,<sup>bb</sup> J. Becker Tjus,<sup>k</sup> S. BenZvi,<sup>as</sup> D. Berley,<sup>q</sup> E. Bernardini,<sup>bc,bd</sup>  
11 D. Z. Besson,<sup>ad,be</sup> G. Binder,<sup>h,i</sup> D. Bindig,<sup>bb</sup> E. Blaufuss,<sup>q</sup> S. Blot,<sup>bc</sup> C. Boehm,<sup>at</sup> M. Börner,<sup>u</sup>  
12 S. Böser,<sup>aj</sup> O. Botner,<sup>ba</sup> J. Böttcher,<sup>a</sup> E. Bourbeau,<sup>t</sup> J. Bourbeau,<sup>ai</sup> F. Bradascio,<sup>bc</sup>  
13 J. Braun,<sup>ai</sup> S. Bron,<sup>z</sup> J. Brostean-Kaiser,<sup>bc</sup> A. Burgman,<sup>ba</sup> J. Buscher,<sup>a</sup> R. S. Busse,<sup>al</sup>  
14 T. Carver,<sup>z</sup> C. Chen,<sup>f</sup> E. Cheung,<sup>q</sup> D. Chirkin,<sup>ai</sup> S. Choi,<sup>av</sup> K. Clark,<sup>ae</sup> L. Classen,<sup>al</sup>  
15 A. Coleman,<sup>am</sup> G. H. Collin,<sup>n</sup> J. M. Conrad,<sup>n</sup> P. Coppin,<sup>m</sup> P. Correa,<sup>m</sup> D. F. Cowen,<sup>ay,az</sup>  
16 R. Cross,<sup>as</sup> P. Dave,<sup>f</sup> C. De Clercq,<sup>m</sup> J. J. DeLaunay,<sup>az</sup> H. Dembinski,<sup>am</sup> K. Deoskar,<sup>at</sup>  
17 S. De Ridder,<sup>aa</sup> P. Desiati,<sup>ai</sup> K. D. de Vries,<sup>m</sup> G. de Wasseige,<sup>m</sup> M. de With,<sup>j</sup> T. DeYoung,<sup>v</sup>  
18 A. Diaz,<sup>n</sup> J. C. Díaz-Vélez,<sup>ai</sup> H. Dujmovic,<sup>av</sup> M. Dunkman,<sup>az</sup> E. Dvorak,<sup>aq</sup> B. Eberhardt,<sup>ai</sup>  
19 T. Ehrhardt,<sup>aj</sup> P. Eller,<sup>az</sup> R. Engel,<sup>ac</sup> P. A. Evenson,<sup>am</sup> S. Fahey,<sup>ai</sup> A. R. Fazely,<sup>g</sup> J. Felde,<sup>q</sup>  
20 K. Filimonov,<sup>h</sup> C. Finley,<sup>at</sup> D. Fox,<sup>ay</sup> A. Franckowiak,<sup>bc</sup> E. Friedman,<sup>q</sup> A. Fritz,<sup>aj</sup>  
21 T. K. Gaisser,<sup>am</sup> J. Gallagher,<sup>ah</sup> E. Ganster,<sup>a</sup> S. Garrappa,<sup>bc</sup> L. Gerhardt,<sup>i</sup> K. Ghorbani,<sup>ai</sup>  
22 T. Glauch,<sup>y</sup> T. Glüsenkamp,<sup>x</sup> A. Goldschmidt,<sup>i</sup> J. G. Gonzalez,<sup>am</sup> D. Grant,<sup>v</sup> Z. Griffith,<sup>ai</sup>  
23 S. Griswold,<sup>as</sup> M. Günder,<sup>a</sup> M. Gündüz,<sup>k</sup> C. Haack,<sup>a</sup> A. Hallgren,<sup>ba</sup> L. Halve,<sup>a</sup> F. Halzen,<sup>ai</sup>  
24 K. Hanson,<sup>ai</sup> A. Haungs,<sup>ac</sup> D. Hebecker,<sup>j</sup> D. Heereman,<sup>l</sup> P. Heix,<sup>a</sup> K. Helbing,<sup>bb</sup> R. Hellauer,<sup>q</sup>  
25 F. Henningsen,<sup>y</sup> S. Hickford,<sup>bb</sup> J. Hignight,<sup>w</sup> G. C. Hill,<sup>b</sup> K. D. Hoffman,<sup>q</sup> R. Hoffmann,<sup>bb</sup>  
26 T. Hoinka,<sup>u</sup> B. Hokanson-Fasig,<sup>ai</sup> K. Hoshina,<sup>ai,be</sup> F. Huang,<sup>az</sup> M. Huber,<sup>y</sup> T. Huber,<sup>ac,bc</sup>  
27 K. Hultqvist,<sup>at</sup> M. Hünnefeld,<sup>u</sup> R. Hussain,<sup>ai</sup> S. In,<sup>av</sup> N. Iovine,<sup>l</sup> A. Ishihara,<sup>o</sup> G. S. Japaridze,<sup>e</sup>  
28 M. Jeong,<sup>av</sup> K. Jero,<sup>ai</sup> B. J. P. Jones,<sup>d</sup> F. Jonske,<sup>a</sup> R. Joppe,<sup>a</sup> D. Kang,<sup>ac</sup> W. Kang,<sup>av</sup>  
29 A. Kappes,<sup>al</sup> D. Kappesser,<sup>aj</sup> T. Karg,<sup>bc</sup> M. Karl,<sup>y</sup> A. Karle,<sup>ai</sup> U. Katz,<sup>x</sup> M. Kauer,<sup>ai</sup>  
30 J. L. Kelley,<sup>ai</sup> A. Kheirandish,<sup>ai</sup> J. Kim,<sup>av</sup> T. Kintscher,<sup>bc</sup> J. Kiryluk,<sup>au</sup> T. Kittler,<sup>x</sup>  
31 S. R. Klein,<sup>h,i</sup> R. Koirala,<sup>am</sup> H. Kolanoski,<sup>j</sup> L. Köpke,<sup>aj</sup> C. Kopper,<sup>v</sup> S. Kopper,<sup>ax</sup>  
32 D. J. Koskinen,<sup>t</sup> M. Kowalski,<sup>j,bc</sup> K. Krings,<sup>y</sup> G. Krückl,<sup>aj</sup> N. Kulacz,<sup>w</sup> N. Kurahashi,<sup>ap</sup>  
33 A. Kyriacou,<sup>b</sup> M. Labare,<sup>aa</sup> J. L. Lanfranchi,<sup>az</sup> M. J. Larson,<sup>q</sup> F. Lauber,<sup>bb</sup> J. P. Lazar,<sup>ai</sup>  
34 K. Leonard,<sup>ai</sup> A. Leszczyńska,<sup>ac</sup> M. Leuermann,<sup>a</sup> Q. R. Liu,<sup>ai</sup> E. Lohfink,<sup>aj</sup>

35 C. J. Lozano Mariscal,<sup>al</sup> L. Lu,<sup>o</sup> F. Lucarelli,<sup>z</sup> J. Lünemann,<sup>m</sup> W. Luszczak,<sup>ai</sup> Y. Lyu,<sup>h,i</sup>  
 36 W. Y. Ma,<sup>bc</sup> J. Madsen,<sup>ar</sup> G. Maggi,<sup>m</sup> K. B. M. Mahn,<sup>v</sup> Y. Makino,<sup>o</sup> P. Mallik,<sup>a</sup> K. Mallot,<sup>ai</sup>  
 37 S. Mancina,<sup>ai</sup> I. C. Mariş,<sup>l</sup> R. Maruyama,<sup>an</sup> K. Mase,<sup>o</sup> R. Maunu,<sup>q</sup> F. McNally,<sup>ag</sup> K. Meagher,<sup>ai</sup>  
 38 M. Medici,<sup>t</sup> A. Medina,<sup>s</sup> M. Meier,<sup>u</sup> S. Meighen-Berger,<sup>y</sup> T. Menne,<sup>u</sup> G. Merino,<sup>ai</sup> T. Meures,<sup>l</sup>  
 39 J. Micallef,<sup>v</sup> D. Mockler,<sup>l</sup> G. Momenté,<sup>aj</sup> T. Montaruli,<sup>z</sup> R. W. Moore,<sup>w</sup> R. Morse,<sup>ai</sup> M. Moulai,<sup>n</sup>  
 40 P. Muth,<sup>a</sup> R. Nagai,<sup>o</sup> U. Naumann,<sup>bb</sup> G. Neer,<sup>v</sup> H. Niederhausen,<sup>y</sup> M. U. Nisa,<sup>v</sup> S. C. Nowicki,<sup>v</sup>  
 41 D. R. Nygren,<sup>i</sup> A. Obertacke Pollmann,<sup>bb</sup> M. Oehler,<sup>ac</sup> A. Olivas,<sup>q</sup> A. O’Murchadha,<sup>l</sup>  
 42 E. O’Sullivan,<sup>at</sup> T. Palczewski,<sup>h,i</sup> H. Pandya,<sup>am</sup> D. V. Pankova,<sup>az</sup> N. Park,<sup>ai</sup> P. Peiffer,<sup>aj</sup>  
 43 C. Pérez de los Heros,<sup>ba</sup> S. Philippen,<sup>a</sup> D. Pieloth,<sup>u</sup> E. Pinat,<sup>l</sup> A. Pizzuto,<sup>ai</sup> M. Plum,<sup>ak</sup>  
 44 A. Porcelli,<sup>aa</sup> P. B. Price,<sup>h</sup> G. T. Przybylski,<sup>i</sup> C. Raab,<sup>l</sup> A. Raissi,<sup>p</sup> M. Rameez,<sup>t</sup> L. Rauch,<sup>bc</sup>  
 45 K. Rawlins,<sup>c</sup> I. C. Rea,<sup>y</sup> R. Reimann,<sup>a</sup> B. Relethford,<sup>ap</sup> M. Renschler,<sup>ac</sup> G. Renzi,<sup>l</sup>  
 46 E. Resconi,<sup>y</sup> W. Rhode,<sup>u</sup> M. Richman,<sup>ap</sup> S. Robertson,<sup>i</sup> M. Rongen,<sup>a</sup> C. Rott,<sup>av</sup> T. Ruhe,<sup>u</sup>  
 47 D. Ryckbosch,<sup>aa</sup> D. Rysewyk,<sup>v</sup> I. Safa,<sup>ai</sup> S. E. Sanchez Herrera,<sup>v</sup> A. Sandrock,<sup>u</sup>  
 48 J. Sandros,<sup>aj</sup> M. Santander,<sup>ax</sup> S. Sarkar,<sup>ao</sup> S. Sarkar,<sup>w</sup> K. Satalecka,<sup>bc</sup> M. Schaufel,<sup>a</sup>  
 49 H. Schieler,<sup>ac</sup> P. Schlunder,<sup>u</sup> T. Schmidt,<sup>q</sup> A. Schneider,<sup>ai</sup> J. Schneider,<sup>x</sup>  
 50 F. G. Schröder,<sup>ac,am</sup> L. Schumacher,<sup>a</sup> S. Sclafani,<sup>ap</sup> D. Seckel,<sup>am</sup> S. Seunarine,<sup>ar</sup>  
 51 S. Shefali,<sup>a</sup> M. Silva,<sup>ai</sup> R. Snihur,<sup>ai</sup> J. Soedingrekso,<sup>u</sup> D. Soldin,<sup>am</sup> M. Song,<sup>q</sup>  
 52 G. M. Spiczak,<sup>ar</sup> C. Spiering,<sup>bc</sup> J. Stachurska,<sup>bc</sup> M. Stamatikos,<sup>s</sup> T. Stanev,<sup>am</sup> R. Stein,<sup>bc</sup>  
 53 P. Steinmüller,<sup>ac</sup> J. Stettner,<sup>a</sup> A. Steuer,<sup>aj</sup> T. Stezelberger,<sup>i</sup> R. G. Stokstad,<sup>i</sup> A. Stöbl,<sup>o</sup>  
 54 N. L. Strotjohann,<sup>bc</sup> T. Stürwald,<sup>a</sup> T. Stuttard,<sup>t</sup> G. W. Sullivan,<sup>q</sup> I. Taboada,<sup>f</sup> F. Tenholt,<sup>k</sup>  
 55 S. Ter-Antonyan,<sup>g</sup> A. Terliuk,<sup>bc</sup> S. Tilav,<sup>am</sup> K. Tollefson,<sup>v</sup> L. Tomankova,<sup>k</sup> C. Tönnis,<sup>aw</sup>  
 56 S. Toscano,<sup>l</sup> D. Tosi,<sup>ai</sup> A. Trettin,<sup>bc</sup> M. Tselengidou,<sup>x</sup> C. F. Tung,<sup>f</sup> A. Turcati,<sup>y</sup> R. Turcotte,<sup>ac</sup>  
 57 C. F. Turley,<sup>az</sup> B. Ty,<sup>ai</sup> E. Unger,<sup>ba</sup> M. A. Unland Elorrieta,<sup>al</sup> M. Usner,<sup>bc</sup> J. Vandenbroucke,<sup>ai</sup>  
 58 W. Van Driessche,<sup>aa</sup> D. van Eijk,<sup>ai</sup> N. van Eijndhoven,<sup>m</sup> S. Vanheule,<sup>aa</sup> J. van Santen,<sup>bc</sup>  
 59 M. Vraeghe,<sup>aa</sup> C. Walck,<sup>at</sup> A. Wallace,<sup>b</sup> M. Wallraff,<sup>a</sup> N. Wandkowsky,<sup>ai</sup> T. B. Watson,<sup>d</sup>  
 60 C. Weaver,<sup>w</sup> A. Weindl,<sup>ac</sup> M. J. Weiss,<sup>az</sup> J. Weldert,<sup>aj</sup> C. Wendt,<sup>ai</sup> J. Werthebach,<sup>ai</sup>  
 61 B. J. Whelan,<sup>b</sup> N. Whitehorn,<sup>af</sup> K. Wiebe,<sup>aj</sup> C. H. Wiebusch,<sup>a</sup> L. Wille,<sup>ai</sup> D. R. Williams,<sup>ax</sup>  
 62 L. Wills,<sup>ap</sup> M. Wolf,<sup>y</sup> J. Wood,<sup>ai</sup> T. R. Wood,<sup>w</sup> K. Woschnagg,<sup>h</sup> G. Wrede,<sup>x</sup> D. L. Xu,<sup>ai</sup>  
 63 X. W. Xu,<sup>g</sup> Y. Xu,<sup>au</sup> J. P. Yanez,<sup>w</sup> G. Yodh,<sup>ab</sup> S. Yoshida,<sup>o</sup> T. Yuan<sup>ai</sup> and M. Zöcklein<sup>a</sup>

64 <sup>a</sup>*III. Physikalisches Institut, RWTH Aachen University, D-52056 Aachen, Germany*

65 <sup>b</sup>*Department of Physics, University of Adelaide, Adelaide, 5005, Australia*

66 <sup>c</sup>*Dept. of Physics and Astronomy, University of Alaska Anchorage, 3211 Providence Dr., Anchorage, AK*  
 67 *99508, USA*

68 <sup>d</sup>*Dept. of Physics, University of Texas at Arlington, 502 Yates St., Science Hall Rm 108, Box 19059,*  
 69 *Arlington, TX 76019, USA*

70 <sup>e</sup>*CTSPS, Clark-Atlanta University, Atlanta, GA 30314, USA*

71 <sup>f</sup>*School of Physics and Center for Relativistic Astrophysics, Georgia Institute of Technology, Atlanta, GA*  
 72 *30332, USA*

73 <sup>g</sup>*Dept. of Physics, Southern University, Baton Rouge, LA 70813, USA*

74 <sup>h</sup>*Dept. of Physics, University of California, Berkeley, CA 94720, USA*

75 <sup>i</sup>*Lawrence Berkeley National Laboratory, Berkeley, CA 94720, USA*

76 <sup>j</sup>*Institut für Physik, Humboldt-Universität zu Berlin, D-12489 Berlin, Germany*

77 <sup>k</sup>*Fakultät für Physik & Astronomie, Ruhr-Universität Bochum, D-44780 Bochum, Germany*

78 <sup>l</sup> *Université Libre de Bruxelles, Science Faculty CP230, B-1050 Brussels, Belgium*  
79 <sup>m</sup> *Vrije Universiteit Brussel (VUB), Dienst ELEM, B-1050 Brussels, Belgium*  
80 <sup>n</sup> *Dept. of Physics, Massachusetts Institute of Technology, Cambridge, MA 02139, USA*  
81 <sup>o</sup> *Dept. of Physics and Institute for Global Prominent Research, Chiba University, Chiba 263-8522, Japan*  
82 <sup>p</sup> *Dept. of Physics and Astronomy, University of Canterbury, Private Bag 4800, Christchurch, New Zealand*  
83 <sup>q</sup> *Dept. of Physics, University of Maryland, College Park, MD 20742, USA*  
84 <sup>r</sup> *Dept. of Astronomy, Ohio State University, Columbus, OH 43210, USA*  
85 <sup>s</sup> *Dept. of Physics and Center for Cosmology and Astro-Particle Physics, Ohio State University, Columbus,*  
86 *OH 43210, USA*  
87 <sup>t</sup> *Niels Bohr Institute, University of Copenhagen, DK-2100 Copenhagen, Denmark*  
88 <sup>u</sup> *Dept. of Physics, TU Dortmund University, D-44221 Dortmund, Germany*  
89 <sup>v</sup> *Dept. of Physics and Astronomy, Michigan State University, East Lansing, MI 48824, USA*  
90 <sup>w</sup> *Dept. of Physics, University of Alberta, Edmonton, Alberta, Canada T6G 2E1*  
91 <sup>x</sup> *Erlangen Centre for Astroparticle Physics, Friedrich-Alexander-Universität Erlangen-Nürnberg, D-91058*  
92 *Erlangen, Germany*  
93 <sup>y</sup> *Physik-department, Technische Universität München, D-85748 Garching, Germany*  
94 <sup>z</sup> *Département de physique nucléaire et corpusculaire, Université de Genève, CH-1211 Genève, Switzerland*  
95 <sup>aa</sup> *Dept. of Physics and Astronomy, University of Gent, B-9000 Gent, Belgium*  
96 <sup>ab</sup> *Dept. of Physics and Astronomy, University of California, Irvine, CA 92697, USA*  
97 <sup>ac</sup> *Karlsruhe Institute of Technology, Institut für Kernphysik, D-76021 Karlsruhe, Germany*  
98 <sup>ad</sup> *Dept. of Physics and Astronomy, University of Kansas, Lawrence, KS 66045, USA*  
99 <sup>ae</sup> *SNOLAB, 1039 Regional Road 24, Creighton Mine 9, Lively, ON, Canada P3Y 1N2*  
100 <sup>af</sup> *Department of Physics and Astronomy, UCLA, Los Angeles, CA 90095, USA*  
101 <sup>ag</sup> *Department of Physics, Mercer University, Macon, GA 31207-0001, USA*  
102 <sup>ah</sup> *Dept. of Astronomy, University of Wisconsin, Madison, WI 53706, USA*  
103 <sup>ai</sup> *Dept. of Physics and Wisconsin IceCube Particle Astrophysics Center, University of Wisconsin, Madison,*  
104 *WI 53706, USA*  
105 <sup>aj</sup> *Institute of Physics, University of Mainz, Staudinger Weg 7, D-55099 Mainz, Germany*  
106 <sup>ak</sup> *Department of Physics, Marquette University, Milwaukee, WI, 53201, USA*  
107 <sup>al</sup> *Institut für Kernphysik, Westfälische Wilhelms-Universität Münster, D-48149 Münster, Germany*  
108 <sup>am</sup> *Bartol Research Institute and Dept. of Physics and Astronomy, University of Delaware, Newark, DE 19716,*  
109 *USA*  
110 <sup>an</sup> *Dept. of Physics, Yale University, New Haven, CT 06520, USA*  
111 <sup>ao</sup> *Dept. of Physics, University of Oxford, Parks Road, Oxford OX1 3PU, UK*  
112 <sup>ap</sup> *Dept. of Physics, Drexel University, 3141 Chestnut Street, Philadelphia, PA 19104, USA*  
113 <sup>aq</sup> *Physics Department, South Dakota School of Mines and Technology, Rapid City, SD 57701, USA*  
114 <sup>ar</sup> *Dept. of Physics, University of Wisconsin, River Falls, WI 54022, USA*  
115 <sup>as</sup> *Dept. of Physics and Astronomy, University of Rochester, Rochester, NY 14627, USA*  
116 <sup>at</sup> *Oskar Klein Centre and Dept. of Physics, Stockholm University, SE-10691 Stockholm, Sweden*  
117 <sup>au</sup> *Dept. of Physics and Astronomy, Stony Brook University, Stony Brook, NY 11794-3800, USA*  
118 <sup>av</sup> *Dept. of Physics, Sungkyunkwan University, Suwon 16419, Korea*  
119 <sup>aw</sup> *Institute of Basic Science, Sungkyunkwan University, Suwon 16419, Korea*  
120 <sup>ax</sup> *Dept. of Physics and Astronomy, University of Alabama, Tuscaloosa, AL 35487, USA*  
121 <sup>ay</sup> *Dept. of Astronomy and Astrophysics, Pennsylvania State University, University Park, PA 16802, USA*

122 <sup>az</sup>*Dept. of Physics, Pennsylvania State University, University Park, PA 16802, USA*

123 <sup>ba</sup>*Dept. of Physics and Astronomy, Uppsala University, Box 516, S-75120 Uppsala, Sweden*

124 <sup>bb</sup>*Dept. of Physics, University of Wuppertal, D-42119 Wuppertal, Germany*

125 <sup>bc</sup>*DESY, D-15738 Zeuthen, Germany*

126 <sup>bd</sup>*also at Università di Padova, I-35131 Padova, Italy*

127 <sup>be</sup>*also at National Research Nuclear University, Moscow Engineering Physics Institute (MEPhI), Moscow*  
128 *115409, Russia*

129 <sup>bf</sup>*Earthquake Research Institute, University of Tokyo, Bunkyo, Tokyo 113-0032, Japan*

130 *E-mail: [analysis@icecube.wisc.edu](mailto:analysis@icecube.wisc.edu)*

131 **ABSTRACT:** This article outlines the in-situ calibration of the single-photoelectron charge distri-  
132 **butions** for each of the Hamamatsu Photonics R7081-02 (MOD) photomultipliers in the IceCube  
133 **Neutrino Observatory.** The accurate characterization of the individual PMT charge distributions is  
134 **important** for event reconstruction and calibration. We discuss the single photoelectron identification  
135 **procedure** and how we extract the single-photoelectron charge distribution using a deconvolution  
136 **of the multiple photoelectron charge distribution,** and we examine various correlations between the  
137 **shape of the single-photoelectron charge distribution and various hardware components.** The time  
138 **dependence of the individual PMT charge distributions is also investigated.**

139 **KEYWORDS:** IceCube, single photoelectron, charge distribution, PMT

140 **ARXIV EPRINT:** [tbd](#)

---

141 **Contents**

142	<b>1 Introduction</b>	<b>1</b>
143	1.1 Single-photoelectron charge distributions	3
144	1.2 IceCube datasets and software definitions	5
145	<b>2 Extracting the SPE templates</b>	<b>6</b>
146	2.1 Single photoelectron pulse selection	6
147	2.2 Characterizing the low-charge region	8
148	2.3 Fitting procedure	9
149	2.4 SPE template fit results	10
150	<b>3 Discussion</b>	<b>10</b>
151	3.1 Correlations between fit parameters and DOM hardware differences	10
152	3.2 Fitting parameters variation over time	13
153	3.3 Quantifying observable changes when modifying the PMT charge distributions	13
154	3.3.1 Model comparison	14
155	3.4 SPE templates in simulation	15
156	3.5 SPE templates for calibration	16
157	<b>4 Conclusion</b>	<b>16</b>

---

158 **1 Introduction**

159 The IceCube Neutrino Observatory [1, 2] is a cubic-kilometer-sized array of 5,160 photomultiplier  
160 tubes (PMTs) buried in the Antarctic ice sheet, designed to observe high-energy neutrinos interacting  
161 with the ice [3]. In 2011, the IceCube Collaboration completed the installation of 86 vertical *strings*  
162 of PMT modules, eight of which were arranged in a denser configuration known as the DeepCore  
163 sub-array [4]. Each string in IceCube contains 60 digital optical modules (DOMs), which contain  
164 a single PMT each, as well as all required electronics [5]. The primary 78 strings (excluding  
165 DeepCore) are spaced 125 m apart in a hexagonal grid, with the DOMs extending from 1450 m to  
166 2450 m below the surface of the ice sheet. The additional DeepCore strings (79-86) are positioned  
167 between the centermost strings in the detector, reducing the horizontal DOM-to-DOM distance in  
168 this region to 42 m and 72 m. The lower 50 DOMs on these strings are located in the deepest 350 m  
169 of the detector near the clearest ice, while the upper ten provide a cosmic ray veto extending down  
170 from 1900 m to 2000 m below the surface.

171 Each DOM consists of a 0.5" thick spherical glass pressure vessel that houses a single down-  
172 facing 10" PMT from Hamamatsu Photonics. The PMT is coupled to the glass housing with optical  
173 gel and is surrounded by a wire mesh of mu metal to reduce the effect of the Earth's ambient  
174 magnetic field. The glass housing is transparent to wavelengths 350 nm and above [6].

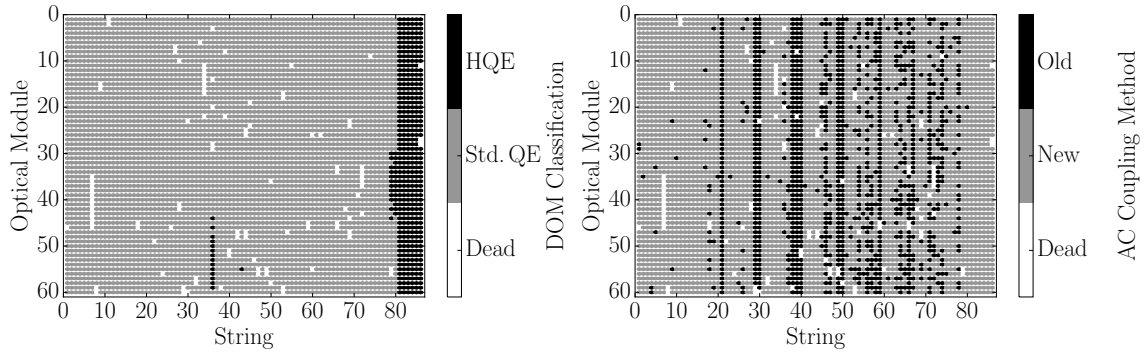


**Figure 1.** Left: A mapping of the HQE (black) and Standard QE DOMs (gray). Right: The version of AC coupling, old toroids (black) and new toroids (gray). DOMs that have been removed from service are shown in white.

175 Of the 5,160 DOMs, 4,762 house a R7081-02 Hamamatsu Photonics PMT, specified for  
 176 wavelengths ranging from 300 nm to 650 nm, with peak quantum efficiency of 25% near 390 nm.  
 177 These are classified as Standard Quantum Efficiency (Standard QE) DOMs. The remaining 398  
 178 DOMs are equipped with the Hamamatsu R7081-02MOD PMTs, which, having a peak quantum  
 179 efficiency of 34% near 390 nm (36% higher efficiency than the Standard QE DOMs), are classified  
 180 as High Quantum Efficiency (HQE) DOMs [4]. These DOMs are primarily located in DeepCore  
 181 and on strings 36 and 43, as shown in the left side of Fig. 1.

182 The R7081-02 and R7081-02MOD PMTs have 10 dynode stages and are operated with a gain  
 183 of  $10^7$  and high voltage around 1200 V. A typical amplified single photoelectron will generate a  
 184  $\sim 6$  mV peak voltage at the input to the front-end amplifiers. The PMTs operate with the anodes at  
 185 high voltage and the signal is AC coupled to the front-end amplifiers. There are two versions of AC  
 186 coupling in the detectors, both of which use custom-designed wideband bifilar wound 1:1 toroidal  
 187 transformers<sup>1</sup>. The locations of DOMs with the different versions of AC-coupling, new and old  
 188 toroids, are shown on the right side of Fig. 1. The DOMs with the old toroids were designed with  
 189 an impedance of 43  $\Omega$ , while the new toroids are 50  $\Omega$  [7]. All HQE DOMs are instrumented with  
 190 the new toroids.

191 IceCube relies on two observables per DOM to reconstruct events: the total number of detected  
 192 photons and their timing distribution. Both the timing and the number of photons are extracted  
 193 from the digitized waveforms. This is accomplished by deconvolving the waveforms into a series of  
 194 scaled single photoelectron pulses (so-called pulse series) and the integral of the individual pulses  
 195 (divided by the load resistance) defines the observed charge. It will often be expressed in units of  
 196 PE, or photoelectrons, which further divides the measured charge by the charge of a single electron  
 197 times the nominal gain ( $10^7$ ). Accurate characterization of the individual PMT charge distributions  
 198 is crucial for calibration and event reconstructions relying on charge information. The charge

<sup>1</sup>Conventional AC-coupling high-voltage ceramic capacitors can produce noise from leakage currents and impractical requirements on the capacitors in order to meet the signal droop and undershoot requirements. The toroidal transformer effectively acts as a high-pass filter with good signal fidelity at high frequencies. It also provides higher reliability than capacitive coupling and reduces the stored energy, which might cause damage if there is HV discharge in the system [6]. However, the toroidal-transformer AC coupling also introduces signal droop and undershoot.

199 distribution can also be used to assess long-term detector performance and identify discrepancies  
200 between data and Monte Carlo. It is therefore critically important to accurately measure the single-  
201 photoelectron (SPE) charge distribution in order to understand the IceCube detector behavior.

202 When one or more photons produce a voltage at the anode sufficient to trigger the onboard  
203 discriminator (set via a DAC to approximately 1.3 mV, or equivalently to 0.25 PE), the signal  
204 acquisition process is triggered. The signal is fed into four parallel input channels. Three of the  
205 channels pass first through a 75 ns delay loop in order to capture the leading edge of the pulse and then  
206 into three high-speed (300 MSPS for 128 samples) 10-bit waveform digitizers (Analog Transient  
207 Waveform Digitizer, ATWD), each of which has a different level of amplification:  $15.7 \pm 0.6$ ,  
208  $1.79 \pm 0.06$ , and  $0.21 \pm 0.01$  [7]. There are also three extra ATWDs on board each DOM: one is  
209 used for calibration and the other two operate in a ping-pong fashion to remove dead time associated  
210 with the readout. The signal to the fourth channel is first shaped and amplified and then fed into a  
211 10-bit fast analog-to-digital converter (fADC) operating at a sampling speed of 40 MSPS. Further  
212 detail regarding the description of the DOM electronics can be found in Refs. [5, 8].

213 This article discusses the accurate determination of how individual DOMs collect charge in  
214 order to improve calibration and the detector description as used in the IceCube Monte Carlo  
215 simulation. It describes the procedure for determining the PMT's gain characteristics as seen in the  
216 SPE charge distributions using in-situ data from the IceCube detectors. The SPE charge distribution  
217 refers to the measured charge probability density function of the individual DOMs generated by  
218 the amplification of a pure sample of single photoelectrons. The extraction of the SPE charge  
219 distribution was recently made possible with the development of two pieces of software:

- 220 1. A specially-designed unbiased pulse selection was developed to reduce the multiple photo-  
221 electron (MPE) contamination while accounting for physical phenomena (e.g., late pulses,  
222 afterpulses, pre-pulses, and baseline shifts) and software-related effects (e.g., pulse splitting).  
223 This is further described in Sec. 2.1.
- 224 2. A fitting procedure was developed that separates the remaining MPE contamination from the  
225 SPE charge distribution by deconvolving the measured charged distribution. This is further  
226 described in Sec. 2.3.

227 By using in-situ data to determine the SPE charge distributions, we accurately represent the  
228 individual PMT response as a function of time, environmental conditions, software version and  
229 hardware differences, and we sample photons uniformly over the surface of the photocathode. This  
230 is beneficial since it also allows us to inspect the stability and long-term behavior of the individual  
231 DOMs, verify previous calibration, and correlate features with specific DOM hardware.

## 232 1.1 Single-photoelectron charge distributions

233 In an idealized scenario, a single photon produces a single photoelectron, which is then amplified  
234 by a known amount and the measured charge corresponds to 1 PE. However, there are many physical  
235 processes that create structure in the measured charge distributions. For example:

- 236 • **Statistical fluctuation due to cascade multiplication** [9]. At every stage of dynode amplifi-  
237 cation, there is a stochastic spread in the number of emitted electrons that make it to the next  
238 dynode. This in turn causes a spread in the measured charge after the gain stage of the PMT.

- 239 • **Photoelectron trajectory.** Some electrons may deviate from the favorable trajectory, re-  
 240 ducing the number of secondaries produced at a dynode or the efficiency to collect them  
 241 on the following dynode. This can occur at any stage, but it has the largest effect on the  
 242 multiplication at the first dynode [10]. The trajectory of a photoelectron striking the first  
 243 dynode will depend on many things, including where on the photocathode it was emitted,  
 244 the uniformity of the electric field, the size and shape of the dynodes [9], and the ambient  
 245 magnetic field [11, 12].
  
- 246 • **Late or delayed pulses.** A photoelectron can elastically or inelastically scatter off the first  
 247 dynode. The scattered electron can then be re-accelerated to the dynode, creating a second  
 248 pulse. The difference in time between the initial pulse and the re-accelerated pulse in the  
 249 R7081-02 PMT was previously measured to be up to 70 ns [6, 13]. The two sub-pulses have  
 250 lower charges, but the sum of the two tends to add up to the original charge. Collecting either  
 251 the initial pulse or the late pulse will result in the charge being reconstructed in the low-PE  
 252 region [14].
  
- 253 • **Afterpulses.** When a photoelectron or the secondary electrons produced during the electron  
 254 cascade gain sufficient energy to ionize residual gas in the PMT, the positively charged ionized  
 255 gas will be accelerated in the electric field towards the photocathode. Upon impact with the  
 256 photocathode, electrons can be again released from the photocathode, creating what is called  
 257 an afterpulse. For the R7081-02 PMTs, the timescale for afterpulses was measured to occur  
 258 from 0.3 to 11  $\mu$ s after the initial pulse, with the first prominent afterpulse peak occurring  
 259 at approximately 600 ns [6]. The spread in the afterpulse time is dependent on the position  
 260 of photocathode, the charge-to-mass ratio of the ion produced, and the electric potential  
 261 distribution[15], whereas the size of the afterpulse is related to the momentum and species  
 262 of the ionized gas and composition of the photocathode [16].
  
- 263 • **Pre-pulses.** If an incident photon passes through the photocathode without interaction and  
 264 strikes one of the dynodes, it can eject an electron that is only amplified by the subsequent  
 265 stages, resulting in a lower measured charge (lower by a factor of approximately 25). For the  
 266 IceCube PMTs, the prepulses have been found to arrive approximately 30 ns before the signal  
 267 from other photoelectrons from the photocathode [6].
  
- 268 • **MPE contamination.** When multiple photoelectrons arrive at the first dynodes within several  
 269 nanoseconds of each other, they can be reconstructed by the software as a single, MPE pulse.
  
- 270 • **Electronic noise.** This refers to the fluctuations in the analog-to-digital converters (ATWDs  
 271 and FADC) and ringing that arises from the electronics.

272 Beyond the physical phenomena above that modify the measured charge distribution, there is  
 273 also a lower limit on the smallest charge that can be extracted. For IceCube, the discriminator limits  
 274 the trigger pulse to be above approximately 0.25 PE, and subsequent pulses in the readout time  
 275 window are subject to a software-defined threshold. The software threshold was set conservatively  
 276 to avoid extracting pulses that originated from electronic noise. This threshold can be modified to  
 277 gain access to lower charge pulses and will be discussed in Sec. 2.2.

278 The standard SPE charge distribution model used by the IceCube Collaboration, known as  
 279 the TA0003 distribution [6], represented the above effects as the sum of an exponential plus a  
 280 Gaussian. The exponential component represented charge of poorly amplified pulses and the  
 281 Gaussian represented the spread in statistical fluctuations due to the cascade multiplication. The  
 282 TA0003 distribution was previously used to describe all the PMTs in the IceCube detectors.

283 Recently, IceCube has performed several lab measurements using the R7081-02 PMTs with  
 284 in-time laser pulses, demonstrating that the in-time charge distribution includes a steeply falling  
 285 low-charge component below the discriminator threshold. To account for this, a new functional form  
 286 including a second exponential was introduced. This form of the charge distribution  $f(q)_{SPE} =$   
 287  $\text{Exp}_1 + \text{Exp}_2 + \text{Gaussian}$ , is referred to as the *SPE template* in this article. Explicitly, it is:

$$f(q)_{SPE} = E_1 e^{-q/w_1} + E_2 e^{-q/w_2} + N e^{-\frac{(q-\mu)^2}{2\sigma^2}}, \quad (1.1)$$

288 where  $q$  represents the measured charge;  $E_1$ ,  $E_2$ , and  $N$  represent normalization factors of each  
 289 components;  $w_1$  and  $w_2$  are the exponential decay widths; and  $\mu$ ,  $\sigma$  are the Gaussian mean and  
 290 width, respectively. This is the assumed functional shape of the SPE charge distributions and the  
 291 components of Eq. 1.1 are determined in this article for all in-ice DOMs. IceCube defines 1 PE as  
 292 the location of the Gaussian mean ( $\mu$ ) and calibrates the gain on the individual PMTs during the  
 293 start of each season to meet this definition. The choice of where we define 1 PE is arbitrary, since  
 294 linearity between the total charge collected and the number of incident photons is satisfied up to  
 295  $\sim 2$  V [7]. This is because the average of the distribution is a set fraction of the Gaussian mean and  
 296 the mean of a  $N$ -fold convolution is the sum of means. Any bias in the total observed charge can be  
 297 absorbed into an efficiency term, such as the quantum efficiency.

## 298 1.2 IceCube datasets and software definitions

299 The largest contribution to the IceCube trigger rate comes from downgoing muons produced in  
 300 cosmic ray induced showers [17]. Cosmic ray muons stopping in the detector cause the individual  
 301 trigger rate to decrease at lower depths. Further, climate variations during the formation of the ice  
 302 sheet caused depth-dependent changes in the optical properties of the ice. The optical properties  
 303 also affect the trigger rate; in particular, the “dust layer” from 2100 to 2200 m below the surface is  
 304 a region in the ice with relatively large scattering and absorption coefficients [18].

305 An induced signal in the PMT that passes through the AC coupling toroid located on the  
 306 base of the PMT is compared to a discriminator threshold. If a DOM and its nearest or next to  
 307 nearest neighbor observe a discriminator threshold crossing within a set time window, a *Hard Local*  
 308 *Coincidence* (HLC) is initiated and the corresponding waveforms are sampled 128 times and read  
 309 out on the three ATWDs.

310 After waveform digitization, there is a correction applied to remove the measured DC base-  
 311 line offset. The signal droop and undershoot introduced by the toroidal transformer AC coupling  
 312 is compensated for in software during waveform calibration by adding the expected temperature-  
 313 dependent reaction voltage of the undershoot to the calibrated waveform. If the undershoot voltage  
 314 drops below 0 ADC counts, the ADC values are zeroed and then compensated for once the wave-  
 315 form is above the minimum ADC input. Scaled single photoelectron pulse shapes (that take into  
 316 account the version of the AC coupling) are then fit to the waveforms using software referred to as

317 "WaveDeform" (waveform unfolding process), which determines the individual pulse time stamps  
318 and charges and populates a pulse series [19].

319 The pulse series used in this analysis come from two datasets provided by IceCube:

- 320 1. The **MinBias dataset**. This dataset records the full waveform readout of randomly-triggered  
321 HLC events at a rate that corresponds on average to 1/1000 events. The largest contribution  
322 to the IceCube trigger rate comes from downgoing muons produced in cosmic-ray-induced  
323 showers [17] and therefore is the largest signal component in this dataset. These muons tend  
324 to have small energies when they reach the detector, thus they produce minimal MPE con-  
325 tamination. The full waveform of these events allows us to extract the raw information about  
326 the individual pulses. This will be used to measure the individual PMT charge distributions.
- 327 2. The **BeaconLaunch dataset**. This is a forced triggered filter that is typically used to monitor  
328 the individual DOM baseline. It includes the full ATWD-window waveform readout. Since  
329 this dataset is forced-triggered, the majority of these waveforms represent baseline fluctuations  
330 with minimal contamination from the occasional coincidental pulse that makes it into the  
331 readout window. This dataset will be used to examine the noise contribution to the charge  
332 distributions. Note: when using this dataset, the weight of every pulse is multiplied by  
333 a factor of 28.4 to account for the livetime difference between the MinBias dataset and the  
334 BeaconLaunch dataset. Weight, in this context, refers to the number of photons in the MinBias  
335 dataset proportional to one photon in the BeaconLaunch dataset for which both datasets have  
336 the same equivalent livetime.

337 This analysis uses the full MinBias and BeaconLaunch datasets from IceCube seasons 2011  
338 to 2016 (subsequently referred to as IC86.2011 to IC86.2016). Seasons in IceCube typically start  
339 in June of the labeled year and end approximately one year later. Calibration is performed at the  
340 beginning of each season.

## 341 2 Extracting the SPE templates

### 342 2.1 Single photoelectron pulse selection

343 The pulse selection is the method used to extract candidate, unbiased, single photoelectron pulses  
344 from data while minimizing the MPE contamination. It avoids collecting afterpulses, rejects late  
345 pulses from the trigger, reassembles late pulses, accounts for the discriminator threshold, reduces  
346 the effect of droop and baseline undershoot, and gives sufficient statistics to perform a season-to-  
347 season measurement. An illustrative diagram of the pulse selection is shown in the left side of  
348 Fig. 2, while a description of the procedure is detailed below.

349 We restrict the pulse selection to only extract information from waveforms in which the trigger  
350 pulse does not exceed 10 mV and no subsequent part of the waveform exceeds 20 mV. This reduces  
351 the effect of the baseline undershoot due to the AC coupling or other artifacts from large pulses.

352 In order to trigger a DOM, the input to the front-end amplifiers must exceed the discriminator  
353 threshold. To avoid the selection bias of the discriminator trigger, we ignore the trigger pulse as well  
354 as the entire first 100 ns of the time window. Ignoring the first 100 ns has the added benefit of also  
355 removing late pulses that could be attributed to the triggering pulse. To ensure we are not accepting

356 afterpulses into the selection, we also enforce the constraint that the pulse of interest (POI) is within  
 357 the first 375 ns of the ATWD time window. This also allows us to examine the waveform up to  
 358 50 ns after the POI. In the vicinity of the POI, we check that WaveDeform did not reconstruct any  
 359 pulses up to 50 ns prior to the POI, or 100 to 150 ns after the POI (the light gray region of Fig. 2  
 360 (left)). This latter constraint is to reduce the probability of accidentally splitting a late pulse in the  
 361 summation window.

362 If a pulse is reconstructed between 100 and 375 ns after the time window is opened and the  
 363 voltage criteria are met, it is accepted as a candidate photoelectron and several checks are performed  
 364 on the waveform prior to and after the pulse. The first check is to ensure that the waveform is near the  
 365 baseline just before the rising edge of the POI. This is accomplished by ensuring that the waveform  
 366 does not exceed 1 mV, 50 to 20 ns prior to the POI, and eliminates cases where the POI is a late  
 367 pulse. We also ensure the waveform returns to the baseline by checking that no ADC measurement  
 368 exceeds 1 mV, 100 to 150 ns after the POI. These constraints are illustrated as the horizontal red  
 369 dotted lines and black arrows in the left side of Fig. 2.

370 If all the above criteria are met, we sum the reconstructed charges from the POI time, given by  
 371 WaveDeform, to +100 ns (the dark gray area in Fig. 2 (left)). This ensures that any nearby pulses  
 372 are either fully separated or fully added. WaveDeform may occasionally split an SPE pulse into  
 373 multiple smaller pulses, therefore it is always critical to perform a summation of the charge within  
 374 a window. The 100 ns summation also means that the pulse selection will occasionally accept MPE  
 375 events.

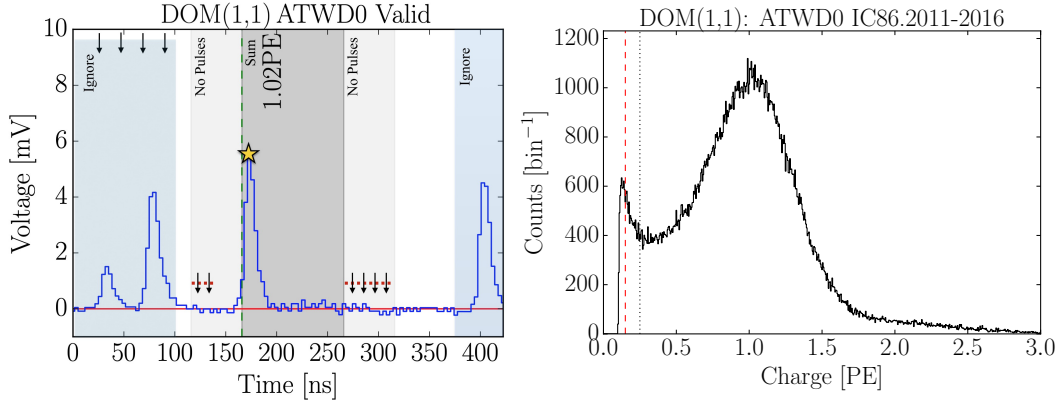


**Figure 2.** Left: An illustrative diagram of the pulse selection criteria for selecting a high-purity and unbiased sample of single photoelectrons. The digitized ATWD waveform is shown in blue. The pulse of interest is identified with a yellow star. This example waveform was triggered by a small pulse at 25 ns (recall that the delay board allows us to examine the waveform just prior to the trigger pulse), followed by a potential late pulse at 70 ns. At 400 ns, we see a pulse in the region susceptible to afterpulses. Waveform voltage checks are illustrated with arrows, and various time windows described in the text are drawn with semi-opaque regions. The POI is reported to have a charge of 1.02 PE, given by WaveDeform, and would pass the pulse selection criteria. Right: The collected charges from string 1, optical module 1 (DOM 1,1), from the MinBias dataset collected from IC86.2011 to IC86.2016 that pass the pulse selection. The discriminator threshold at 0.25 PE is represented as a dotted black vertical line. For visual purposes, a vertical dashed red line is also included at 0.15 PE.

## 376 2.2 Characterizing the low-charge region

377 Fig. 2 (right) shows the charge distributions of the selected pulses that pass the single photoelectron  
 378 pulse selection for string 1, optical module 1, DOM(1,1). In the low-charge region (below 0.25 PE),  
 379 we see a second threshold at approximately 0.13 PE. This is a software-defined threshold that comes  
 380 from a gradient-related termination condition in WaveDeform. The threshold was set to avoid  
 381 electronic noise being interpreted as PMT pulses and contaminating the low-charge region.

382 The steeply falling component of the region from 0.13 PE to 0.25 PE is in agreement with the  
 383 in-time laser tests mentioned in Sec. 1.1 and emphasizes the importance of collecting data below  
 384 the discriminator. This section will assess the noise contribution to this region and examine the  
 385 effect on the charge distribution and noise contribution by lowering the WaveDeform threshold.

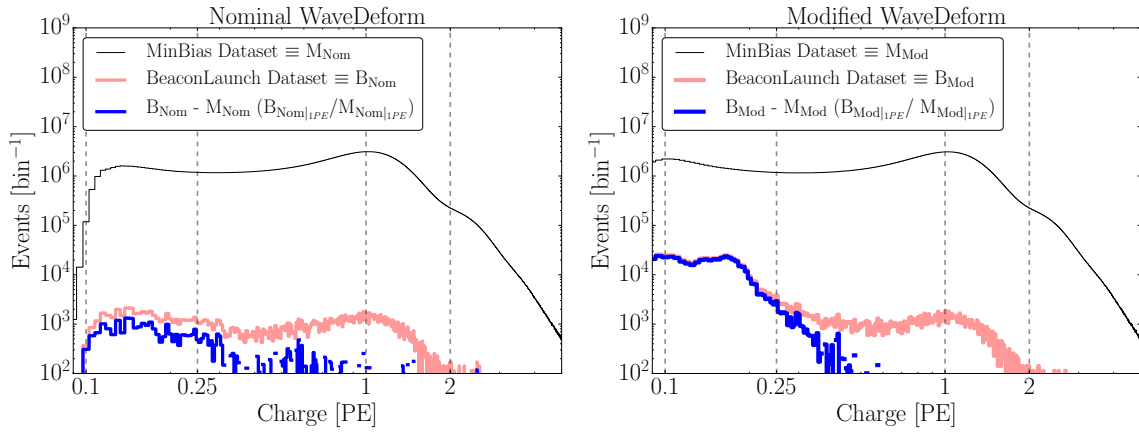


**Figure 3.** The cumulative charge distributions of all DOMs for the MinBias and BeaconLaunch datasets. The blue histogram shows the expected contribution from noise. This was found by subtracting the shape of the MinBias dataset from the BeaconLaunch dataset. Left: The charge distributions for the standard WaveDeform settings. Right: The charge distributions for the modified WaveDeform settings.

386 Fig. 3 (left) shows the charge distributions for the MinBias (black) and the BeaconLaunch  
 387 (red) datasets using the default settings of WaveDeform. As mentioned in Sec. 1.2, occasionally  
 388 a photoelectron will be coincident with the forced BeaconLaunch time window. These charges  
 389 populate a SPE distribution. Subtracting the shape of the MinBias charge distribution from the  
 390 BeaconLaunch dataset yields an estimate of the amount of electronic noise contamination (blue).  
 391 The bin with the largest signal-to-noise ratio (SNR) above 0.1 PE was found to have a SNR of  
 392 0.0013. The SNR for the full distribution was found to be 0.0005. Fig. 3 (right) shows the same  
 393 data after lowering the WaveDeform threshold. Correspondingly, the bin with the largest SNR was  
 394 found to have a SNR of 0.017, whereas the total SNR was found to be 0.0015.

395 The modified WaveDeform datasets show a minimal increase in the contribution of noise to  
 396 the low-charge region. From this, we are able to extract charge information down to approximately  
 397 0.10 PE and improve the overall description of the charge distribution below the discriminator. This  
 398 will help constrain the values defining  $\text{Exp}_1$ .

### 399 2.3 Fitting procedure

400 The fit assumes that there is a negligible three-PE contribution, which is justified by the lack of  
 401 statistics in the 3 PE region as well as the significant rate difference between the 1 PE and 2 PE  
 402 region, as shown in Fig. 2 (right). The 2 PE charge distribution is assumed to be the SPE charge  
 403 distribution convolved with itself [20]. A python-based piece of software called the "convolutional  
 404 fitter" is used to determine the components of Eq. 1.1 from the measured charge distribution that  
 405 includes the MPE contamination.

406 The  $\text{Exp}_2$  component, as well as the  $\text{Exp}_1$ , of Eq. 1.1 represent poorly amplified photoelectrons,  
 407 and we do not allow it to extend beyond the high-charge region of the Gaussian component. In  
 408 particular, we include a constraint on the parameter  $w_2$  to ensure that it falls off with the Gaussian  
 409 component:

$$w_2 < \frac{\mu + 2\sigma}{4 - \text{Ln}(N/E_2)}. \quad (2.1)$$

410 This equation was found by setting the  $\text{Exp}_2$  to be  $1/e^2$  that of the Gaussian component at two sigma  
 411 (the  $\text{Exp}_1$  is neglected from this equation since it falls off in the low-charge region). Eq. 2.1 is used  
 412 as a constraint during the fit to the charge distributions.

413 Pulses that fall below the WaveDeform threshold and are not reconstructed contribute to an  
 414 effective efficiency of the individual DOMs. This analysis assumes the same shape of the steeply  
 415 falling exponential component ( $\text{Exp}_1$ ) for all DOMs in the detector to avoid large fluctuations in  
 416 the individual DOM efficiencies. The modified WaveDeform data will strictly be used to determine  
 417 the  $\text{Exp}_1$  component. Specifically, using the modified WaveDeform, we will background-subtract  
 418 the BeaconLaunch distribution from the MinBias data, fit the resulting distribution to determine  
 419 the components of Eq. 2.1, and use only the measured shape and normalization of  $\text{Exp}_1$  in all  
 420 subsequent unmodified WaveDeform fits.

421 As described in Sec. 1.1, the Gaussian mean ( $\mu$ ) is used to determine the gain setting for each  
 422 PMT. Therefore, it is particularly important that the fit quality in this region accurately describes the  
 423 data. While fitting to the full charge distribution improves the overall fit agreement, the mismatch  
 424 between the chosen functional form (Eq. 1.1) and a true SPE charge distribution can cause the  
 425 Gaussian component to pull away from its ideal location. To compensate for this, the convolutional  
 426 fitter prioritizes fitting to the data around the Gaussian mean. This is accomplished by first fitting  
 427 to the full distribution to get an estimate of the Gaussian mean location. Then, the statistical  
 428 uncertainty is reduced in the region  $\pm 0.15$  PE around the original estimated Gaussian mean, and  
 429 the distribution is re-fitted.

430 Upon fitting the MinBias data with the predetermine values for  $\text{Exp}_1$ , the residual of each  
 431 fit is calculated by measuring the percentage difference between the fit and the data. The average  
 432 residual will then be used as a global scaling factor for all SPE templates to account for the difference  
 433 between the chosen model (Eq. 2.1) and the actual data.

434 All the DOMs with "failed fits" are not included in this article. A DOM is classified as having  
 435 a failed fit if it does not pass one of the validity checks on the data requirements (e.g. number  
 436 of valid pulses) or goodness of fit. The majority of these DOMs have been removed from service  
 437 (approximately 109 DOMs) and the remaining approximately 6 DOMs are known to have various  
 438 issues. In the IceCube MC simulation chain, these DOMs are assigned the average SPE template.

## 439 2.4 SPE template fit results

440 Using the background-subtracted modified WaveDeform  
 441 dataset, the  $\text{Exp}_1$  component was determined by fitting  
 442 the distribution from 0.1 PE to 3.5 PE. The result of the  
 443 fit yielded  $E_1 = 6.9 \pm 1.5$  and  $w_1 = 0.032 \pm 0.002$  PE. The  
 444 shape of  $\text{Exp}_1$  is then used to describe the low-PE charge  
 445 region for all subsequent fits.

446 Using the MinBias dataset with the measured val-  
 447 ues of  $\text{Exp}_1$ , the SPE templates are extracted for every  
 448 DOM, separately for each IceCube season (IC86.2011 to  
 449 IC86.2016). The fit range for  $\text{Exp}_2$  and the Gaussian com-  
 450 ponents is selected to be between 0.15 PE and 3.5 PE. An  
 451 average fit was also performed on the cumulative charge  
 452 distribution, in which all the data for a given DOM was  
 453 summed together (labeled as "AVG").

454 We can divide the DOMs into subsets of hardware differences: the HQE DOMs with the new  
 455 toroids, the Standard QE DOMs with the new toroids, and the Standard QE DOMs with the old  
 456 toroids. The mean value and standard error of the IC86.AVG fit parameters, excluding  $\text{Exp}_1$ , for  
 457 the subset of hardware differences are listed in Table 1. The average residual for all DOMs from 0  
 458 to 1 PE is shown in Fig. 4.

Hardware Configuration	$\text{Exp}_2$ Amp. ( $E_2$ )	$\text{Exp}_2$ Width ( $w_2$ )	Gaus. Amp. ( $N$ )	Gaus. Mean ( $\mu$ )	Gaus. Width ( $\sigma$ )
HQE / New Toroid	$0.644 \pm 0.003$	$0.405 \pm 0.003$	$0.715 \pm 0.002$	$1.0202 \pm 0.0010$	$0.311 \pm 0.001$
Std. QE / New Toroids	$0.566 \pm 0.001$	$0.403 \pm 0.001$	$0.751 \pm 0.001$	$1.0238 \pm 0.0004$	$0.316 \pm 0.001$
Std. QE / Old Toroids	$0.525 \pm 0.002$	$0.420 \pm 0.002$	$0.813 \pm 0.002$	$1.0074 \pm 0.0007$	$0.294 \pm 0.001$

**Table 1.** The average values and standard error of each fit parameter for the subset of hardware configurations listed in the first column.

459 An example fit is shown in Fig. 5 for the cumulative charge distribution for DOM (1,1). The  
 460 collected charge distribution is shown in the black histogram, while the convolutional fit is shown  
 461 as the black line (multiplied by the residual). The extracted SPE template (also multiplied by the  
 462 residual) for this DOM is shown in blue.

## 463 3 Discussion

### 464 3.1 Correlations between fit parameters and DOM hardware differences

465 It is evident from the data provided in Table 1 that the average shape of the SPE templates is dependent  
 466 on the DOM hardware. Most notably, when we examine the subset of DOMs instrumented with  
 467 the new toroids, the average HQE DOM were found to have a particularly larger  $E_2$  component  
 468 ( $13.8 \pm 0.6\%$ ) and smaller Gaussian amplitude ( $-4.77 \pm 0.03\%$ ). Consequently, the average HQE  
 469 peak-to-valley ratio is measured to be  $2.322 \pm 0.013$ , corresponding to  $-12.12 \pm 0.06\%$  lower than  
 470 the average Standard QE DOMs. Also, interestingly, the mean charge of the average HQE DOM

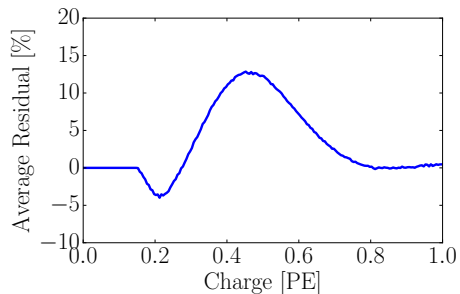


**Figure 4.** The measured average residual of the SPE templates fit.

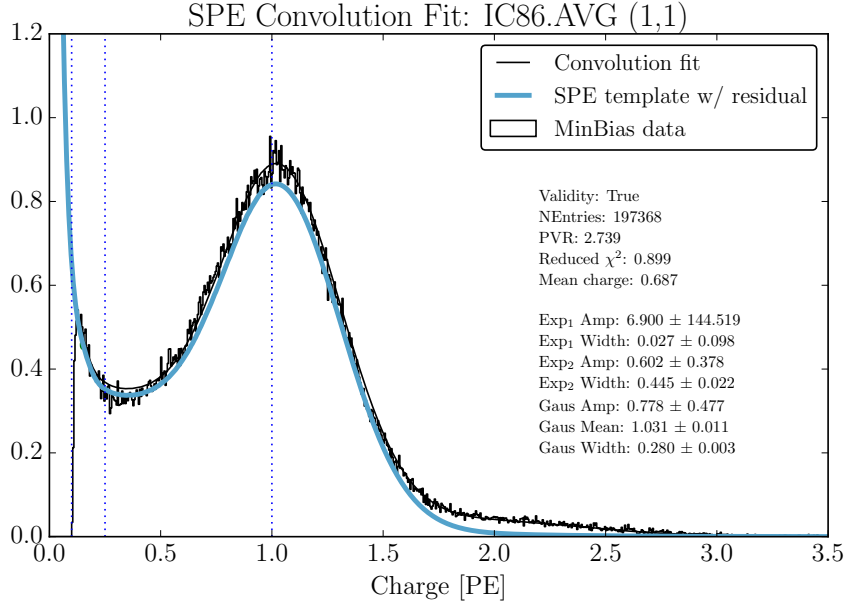


**Figure 5.** An example fit including the residual correction for DOM(1,1) using the WaveDeform dataset for seasons IC86.2011 to IC86.2016. The result from the convolutional fitter is shown as a solid black line. The extracted SPE template is shown blue.

471 was found to be  $-3.34 \pm 0.01\%$  lower than for the Standard QE DOMs. IceCube compensates for  
 472 the change in the mean measured charge in simulation, by increasing the HQE DOM efficiency by  
 473 the equivalent amount. This ensures that the total amount of charge collected by the HQE DOMs  
 474 remains the same prior to, and after, inserting the SPE templates into simulation.

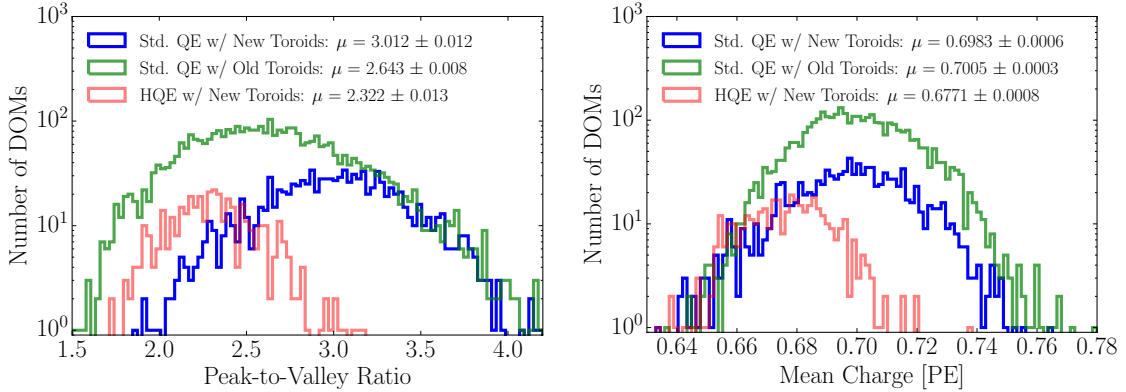


**Figure 6.** Comparison between the R7081-02MOD HQE DOMs and standard R7081-02 DOMs. Left: The peak-to-valley ratio for the two subsets of quantum efficiencies. Right: The mean charge of the individual DOM SPE templates.

475 Similarly, using only the subset of Standard QE DOMs, the SPE templates comparing the  
 476 method of AC coupling were found to have a measurably different shapes. The average Gaus-  
 477 sian amplitude and width for the DOMs instrumented with the old toroids were found to be

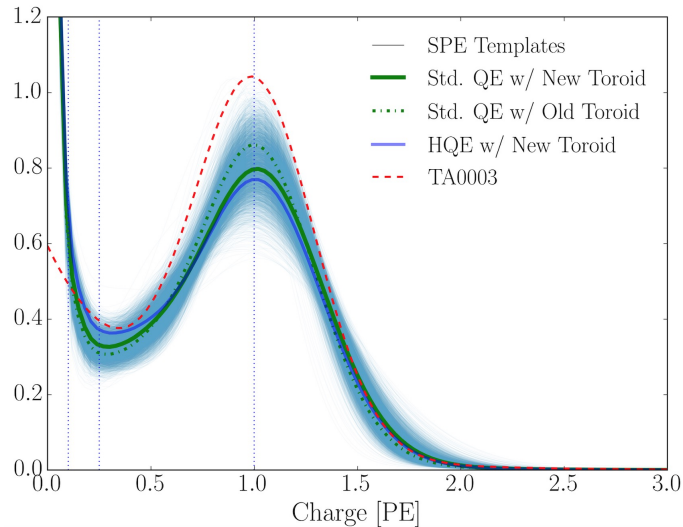


**Figure 7.** A comparison between the SPE templates (light blue band) and the TA0003 (dashed red line) distribution. The average SPE template for the Standard QE and HQE DOMs is shown as the thick blue and green lines, respectively. The SPE templates include the residual correction, and all curves are normalized.

478  $+8.31 \pm 0.01\%$  and  $-6.80 \pm 0.03\%$ , respectively. With these differences, we find a peak-to-valley  
 479 ratio of  $2.643 \pm 0.008$  for the old toroid DOMs and  $3.012 \pm 0.012$  for the new toroid DOMs. The  
 480 average Gaussian mean of the fit for the DOMs with the old toroids was also found to be  $-1.6 \pm 0.1\%$   
 481 lower than those with the new toroids. This corresponds proportionally to a change in the expected  
 482 gain. The mean charge, however, between these two hardware configurations remains very similar  
 483 ( $-0.346 \pm 0.001\%$ ).

484 Although the DOMs instrumented with the old toroids were deployed into the ice earlier  
 485 than those with the new toroids, the differences above is still noted when examining individual  
 486 deployment years; therefore, the shape differences are not attributed to the change in the DOM  
 487 behavior over time. The DOMs with the old toroids were the first PMTs to be manufactured by  
 488 Hamamatsu, so this difference may also be attributed to a gradual change in the process parameters  
 489 over the course of PMT manufacturing, i.e. a change in the production procedure rather than the  
 490 actual AC coupling version. It is also possible that the differences originate from the transfer  
 491 function that models a single photoelectron waveform used in WaveDeform.

492 Fig. 6 shows the distribution of the measured peak-to-valley ratios and mean charge for the  
 493 three different subsets of DOM hardware.

494 Fig. 7 illustrates the average shape differences in the measured SPE templates between the  
 495 HQE DOM with the new toroids (thick blue line), Standard QE with the new toroids (thick green  
 496 line), Standard QE with the old toroids (dash-dot green line), compared to the measured SPE  
 497 templates from the AVG charge distributions (thick blue lines). The figure also shows how the  
 498 TA0003 distribution compares to this recent measurement. The shape difference in the TA0003 is  
 499 attributed to better control of the low-charge region, the difference in functional form (described in  
 500 Section 1.1), and the fact that the SPE templates sample uniformly over the entire photocathode at

501 random incident angles.

### 502 3.2 Fitting parameters variation over time

503 The SPE templates were extracted for each IceCube season independently to investigate the time  
 504 dependence of the fit parameters. For every DOM in the detector, the change over time of each  
 505 fit parameter (excluding  $\text{Exp}_1$ ) was calculated. Fig. 8 shows the change in a given fit parameter,  
 506 relative to the mean value, per year. The measured distribution was found to be consistent with  
 507 statistically scrambling the yearly measurements. The average of each fit parameters are found to  
 508 deviate less than 0.1%, which is in agreement with the stability checks performed in Ref. [7]. This  
 509 observation holds for the individual subset of DOMs with different hardware configurations as well.

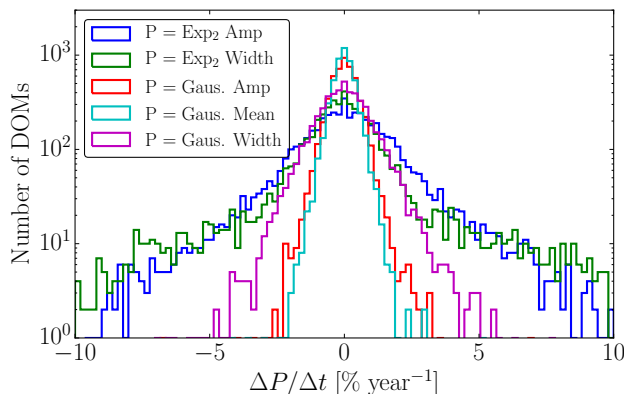


**Figure 8.** The change in the individual DOM fitted parameters over time, represented as percentage deviation from the mean fit parameter value.

### 510 3.3 Quantifying observable changes when modifying the PMT charge distributions

511 Changing the assumed gain response in simulation, as deduced from data, has different implications  
 512 depending on the typical illumination level present in different analyses. These differences are  
 513 outlined in the following discussion.

514 The PMT response is described by a combination of a "bare" efficiency,  $\eta_0$ , and a normalized  
 515 charge response function,  $f(q)$ . The bare efficiency represents the fraction of arriving photons that  
 516 result in any nonzero charge response, including those well below the discriminator threshold. The  
 517 normalization condition is:

$$\int_0^{\text{inf}} f(q) dq = 1. \quad (3.1)$$

518 Generally,  $f(q)$  and  $\eta_0$  have to be adjusted together to maintain agreement with a quantity known  
 519 from lab or in-ice measurements, such as the predicted number of pulses above threshold for a dim  
 520 source.

521 **Dim source measurements** Where light levels are low enough, sub-discriminator pulses do not  
 522 contribute any observed charge because they do not satisfy the trigger threshold, and the probability  
 523 of two photons arriving together is negligible. Given some independent way of knowing the number

524 of arriving photons, a lab or in-ice measurement determines the trigger fraction above threshold  
 525  $\eta_{0.25}$  and/or the average charge over threshold  $Q_{0.25}$ , either of which can be used to constrain the  
 526 model as follows:

$$\eta_{0.25} = \eta_0 \int_{0.25q_{pk}}^{\text{inf}} f(q) dq \quad (3.2)$$

$$Q_{0.25} = \eta_0 \int_{0.25q_{pk}}^{\text{inf}} qf(q) dq \quad (3.3)$$

527 Here, the discriminator threshold is assumed to be 0.25 times the peak position  $q_{pk}$ . It is also  
 528 useful to multiply observed charges by  $q_{pk}$ , since we set each PMT gain by such a reference, and  
 529 then a measurement constraint would be stated in terms of  $Q_{0.25}/q_{pk}$ .

530 **Semi-bright source measurements** Once the ATWD window is open, subsequent pulses are not  
 531 limited by the discriminator threshold. WaveDeform introduces a software termination condition at  
 532 0.1 PE (described at the end of Section 2.1). The average charge of an individual pulse that arrives  
 533 within the time window is:

$$Q_{0.10} = \eta_0 \int_{0.10q_{pk}}^{\text{inf}} qf(q) dq \quad (3.4)$$

534 **Bright source measurements** For light levels that are large, the trigger is satisfied regardless  
 535 of the response to individual photons, and the total charge per arriving photon therefore includes  
 536 contributions below both the discriminator and the WaveDeform thresholds:

$$Q_0 = \eta_0 \int_0^{\text{inf}} qf(q) dq \quad (3.5)$$

537 As such, the total charge is directly proportional to the average charge of the SPE template,  
 538 having a strong dependence on  $\text{Exp}_1$ .

### 539 3.3.1 Model comparison

540 When the charge distribution model is changed in a way that preserves agreement with the measured  
 541  $\eta_{0.25}$  or  $Q_{0.25}/q_{pk}$ , i.e.,  $\eta_0$  is adjusted properly for changes in  $f(q)$ , the physical effect can be  
 542 summarized by the change in the bright-to-dim ratios  $Q_0/Q_{0.25}$ , and  $Q_0/Q_{0.10}$ . Conveniently, these  
 543 ratios depend only on the shape of  $f(q)$ . Table 2 compares these ratios in terms of the TA0003  
 544 charge distribution and the SPE templates described here. It is shown that there are sub-percent  
 545 level differences in the physically-observable bright-to-dim ratios.

Model	Detector	$Q_0/Q_{0.25}$	$Q_0/Q_{0.10}$	$\eta_{0.25}/Q_{0.25}$
TA0003	All DOMs	1.017	1.0031	1.05
SPE Templates	HQE + New Toroids	1.021±0.002	1.0041±0.0004	1.05±0.02
	Std. QE + New Toroids	1.018±0.002	1.0035±0.0005	1.03±0.02
	Std. QE + Old Toroids	1.017±0.002	1.0033±0.0005	1.05±0.02

**Table 2.** The distribution in bright-to-dim ratios for the previous charge distribution (TA0003) and the individual DOM SPE templates for the IceCube and DeepCore detectors.

### 546 3.4 SPE templates in simulation

547 The IceCube Monte Carlo simulation chain assigns a charge to every photoelectron generated at  
 548 the surface of the photocathode. The charge is determined by sampling from a normalized charge  
 549 distribution probability density function. A comparison between describing the charge distribution  
 550 using the SPE templates and the TA0003 distribution follows.

551 Two simulation sets consisting of the same events were processed through the IceCube Monte  
 552 Carlo simulation chain to the final analysis level of an update to the IC86.2011 sterile neutrino analy-  
 553 sis [21]. Here, the events that pass the cuts are  $>99.9\%$  pure upgoing (a trajectory oriented upwards  
 554 relative to the horizon) secondary muons produced by charged current muon neutrino/antineutrino  
 555 interactions. The muon energy range of this event selection is between approximately 500 GeV and  
 556 10 TeV.

557 Fig. 9 (left) shows the distribution of the total measured charge in a single DOM during each  
 558 event. The data is shown for the full IC86.2012 season but is statistically equivalent to any of the  
 559 other seasons. The simulation set using the TA0003 charge distribution is shown in orange, and that  
 560 using the SPE templates is shown in blue. The bottom of the plot shows the ratio of the measured  
 561 quantity relative to data. Fig. 9 (right) shows the distribution of the measured total charge on a  
 562 DOM (after noise removal) divided by the number of channels, or DOMs, that participated in the  
 563 event. Both plots in Fig. 9 have been normalized such that the area under the histograms is the  
 564 same.

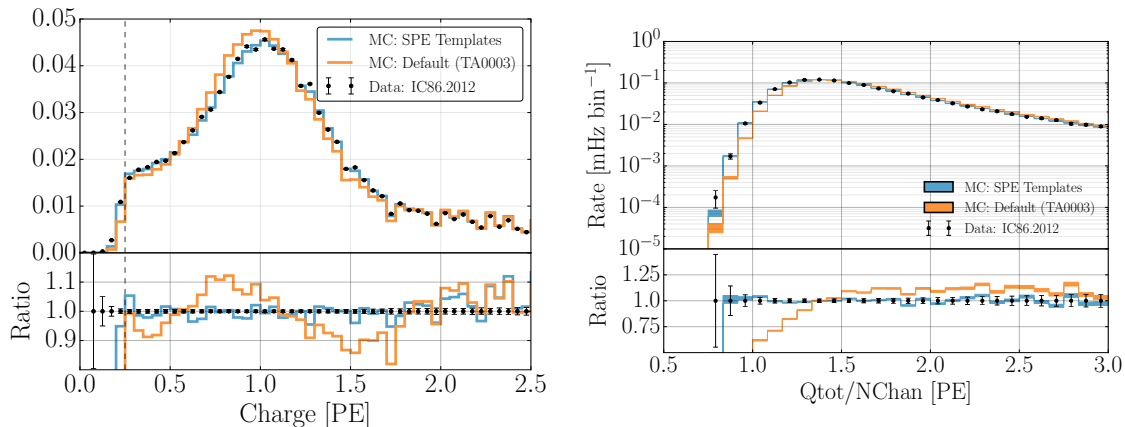


**Figure 9.** A comparison between the SPE templates (blue) and the TA0003 (orange) model for describing the SPE charge distribution in Monte Carlo. The simulation is compared to the 2012 IceCube season. Left: The total measured charge per DOM, per event at analysis level. Right: The distribution of the total measured charge of an event divided by the number of DOMs that participated in the event.

565 The SPE templates clearly improve the overall MC description of these two variables. IceCube  
 566 includes a systematic uncertainty in all analyses, which scales the DOM efficiency to account for  
 567 effects that change the total observed charge. This systematic compensates for the overall mean  
 568 charge shift introduced using the SPE templates; however, the SPE templates now introduce DOM-  
 569 to-DOM differences. This is not expected to change the IceCube physics results since analyses are  
 570 sensitive to the overall detector performance rather than the individual DOM variations.

### 571 **3.5 SPE templates for calibration**

572 The gain setting on each DOM is calibrated at the beginning of the season such that the Gaussian  
573 mean charge distribution corresponds to a gain of  $10^7$ , or equivalently 1 PE. Since the method used  
574 to extract the Gaussian mean described in this article is different from the previous method used  
575 for calibration of the DOMs, the total measured charge from a DOM is expected to change with the  
576 updated calibration.

577 The Gaussian mean component of the fit of every year is found to be on average  $2.00 \pm 0.03\%$   
578 higher than unity with a standard deviation of  $3.54\%$ , corresponding to a systematic overestimation  
579 of the measured charge in the detector. This correction to the measured charge can be implemented  
580 retroactively by dividing the reported charge from WaveDeform by the corresponding Gaussian  
581 mean for a given DOM. Alternatively, the MC can account for this difference by simply inserting  
582 the SPE templates with Gaussian mean matching the values found in the data. Both of these  
583 solutions will be used in future IceCube data/MC production.

## 584 **4 Conclusion**

585 This article outlines the procedure used for collecting a high purity sample of single photoelectron  
586 charges for each of the in-ice DOMs in IceCube. Multiple photoelectron contamination was removed  
587 under the assumption that it is represented by the convolution of the SPE distribution multiple times.

588 The SPE templates were extracted for each season in the IceCube detector and investigated  
589 for time dependent behaviour and correlations with hardware-related features. No significant  
590 time dependence in any of the fitted parameters over the investigated seasons was observed, in  
591 agreement with Ref. [7]. Variations in the fit parameters were found to be consistent with statistical  
592 fluctuations. The HQE DOMs were found to have a smaller peak-to-valley ratio than the Standard  
593 QE DOMs, as well as an overall  $-3.34 \pm 0.01\%$  lower mean charge. It was also found that the  
594 DOMs instrumented with the old toroids used for AC coupling had narrower and larger Gaussian  
595 component corresponding resulting in an increased peak-to-valley ratio of  $14.0 \pm 0.6\%$ .

596 The SPE templates were implemented into the MC simulation production chain and the results  
597 were compared to the default PMT charge distribution (TA0003). A significant improvement in  
598 the description of the low-level variables, total charge per DOM and total charge per event over the  
599 number of channels, was shown. After accounting for SPE templates, the effect on physics analysis,  
600 however, as shown by the bright-to-dim ratios, is expected to be minimal.

601 The new method for extracting the calibration constant that determines the gain setting on each  
602 of the PMTs (the Gaussian mean of the fit) has been revised and shows that the average gain was  
603  $2.00 \pm 0.03\%$  larger than expected. The SPE templates account for this shift in simulation. Previous  
604 physics analyses are not expected to be impacted by this since IceCube includes a systematic  
605 uncertainty that scales the bare efficiency of the DOMs with a prior defined sufficiently large to  
606 absorb this effect. Future reprocessing of the IceCube data will take this shift into account.

607 **Acknowledgments**

608 We acknowledge the support from the following agencies:

609 USA – U.S. National Science Foundation-Office of Polar Programs, U.S. National Science  
610 Foundation-Physics Division, Wisconsin Alumni Research Foundation, Center for High Throughput  
611 Computing (CHTC) at the University of Wisconsin-Madison, Open Science Grid (OSG), Extreme  
612 Science and Engineering Discovery Environment (XSEDE), U.S. Department of Energy-National  
613 Energy Research Scientific Computing Center, Particle astrophysics research computing center at  
614 the University of Maryland, Institute for Cyber-Enabled Research at Michigan State University, and  
615 Astroparticle physics computational facility at Marquette University; Belgium – Funds for Scien-  
616 tific Research (FRS-FNRS and FWO), FWO Odysseus and Big Science programmes, and Belgian  
617 Federal Science Policy Office (Belspo); Germany – Bundesministerium für Bildung und Forschung  
618 (BMBF), Deutsche Forschungsgemeinschaft (DFG), Helmholtz Alliance for Astroparticle Physics  
619 (HAP), Initiative and Networking Fund of the Helmholtz Association, Deutsches Elektronen Syn-  
620 chrotron (DESY), and High Performance Computing cluster of the RWTH Aachen; Sweden –  
621 Swedish Research Council, Swedish Polar Research Secretariat, Swedish National Infrastructure  
622 for Computing (SNIC), and Knut and Alice Wallenberg Foundation; Australia – Australian Re-  
623 search Council; Canada – Natural Sciences and Engineering Research Council of Canada, Calcul  
624 Québec, Compute Ontario, Canada Foundation for Innovation, WestGrid, and Compute Canada;  
625 Denmark – Villum Fonden, Danish National Research Foundation (DNRF), Carlsberg Foundation;  
626 New Zealand – Marsden Fund; Japan – Japan Society for Promotion of Science (JSPS) and Institute  
627 for Global Prominent Research (IGPR) of Chiba University; Korea – National Research Foundation  
628 of Korea (NRF); Switzerland – Swiss National Science Foundation (SNSF); United Kingdom –  
629 Department of Physics, University of Oxford.

630 **References**

- 631 [1] J. Ahrens et al., *Icecube preliminary design document*, URL: <http://www.icecube.wisc.edu/science/publications/pdd> (2001) .
- 632
- 633 [2] A. Achterberg, M. Ackermann, J. Adams, J. Ahrens, K. Andeen, D. Atlee et al., *First year*  
634 *performance of the icecube neutrino telescope*, *Astroparticle Physics* **26** (2006) 155–173.
- 635 [3] I. Collaboration et al., *Evidence for high-energy extraterrestrial neutrinos at the icecube detector*,  
636 *Science* **342** (2013) 1242856.
- 637 [4] R. Abbasi, Y. Abdou, T. Abu-Zayyad, M. Ackermann, J. Adams, J. Aguilar et al., *The design and*  
638 *performance of icecube deepcore*, *Astroparticle physics* **35** (2012) 615–624.
- 639 [5] R. Abbasi, M. Ackermann, J. Adams, M. Ahlers, J. Ahrens, K. Andeen et al., *The icecube data*  
640 *acquisition system: Signal capture, digitization, and timestamping*, *Nuclear Instruments and Methods*  
641 *in Physics Research Section A: Accelerators, Spectrometers, Detectors and Associated Equipment* **601**  
642 (2009) 294–316.
- 643 [6] R. Abbasi, Y. Abdou, T. Abu-Zayyad, J. Adams, J. Aguilar, M. Ahlers et al., *Calibration and*  
644 *characterization of the icecube photomultiplier tube*, *Nuclear Instruments and Methods in Physics*  
645 *Research Section A: Accelerators, Spectrometers, Detectors and Associated Equipment* **618** (2010)  
646 139–152.
- 647 [7] M. Aartsen et al., *The icecube neutrino observatory: Instrumentation and online systems*, *jinst* **12**  
648 (03)(2017) p03012, *arXiv preprint arXiv:1612.05093* 1748–0221.
- 649 [8] R. Stokstad, *Design and performance of the icecube electronics*, .
- 650 [9] Hamamatsu, *Resources: Basics and applications*, URL:  
651 [https://www.hamamatsu.com/resources/pdf/etd/PMT\\_handbook\\_v3aE.pdf](https://www.hamamatsu.com/resources/pdf/etd/PMT_handbook_v3aE.pdf) (2018) .
- 652 [10] Hamamatsu, *Handbook resources, chapter 4*, URL:  
653 [https://www.hamamatsu.com/resources/pdf/etd/PMT\\_handbook\\_v3aE-Chapter4.pdf](https://www.hamamatsu.com/resources/pdf/etd/PMT_handbook_v3aE-Chapter4.pdf) (2018) .
- 654 [11] J. Brack, B. Delgado, J. Dhooghe, J. Felde, B. Gookin, S. Grullon et al., *Characterization of the*  
655 *hamamatsu r11780 12 in. photomultiplier tube*, *Nuclear Instruments and Methods in Physics Research*  
656 *Section A: Accelerators, Spectrometers, Detectors and Associated Equipment* **712** (2013) 162–173.
- 657 [12] E. Calvo, M. Cerrada, C. Fernández-Bedoya, I. Gil-Botella, C. Palomares, I. Rodríguez et al.,  
658 *Characterization of large-area photomultipliers under low magnetic fields: Design and performance*  
659 *of the magnetic shielding for the double chooz neutrino experiment*, *Nuclear Instruments and Methods*  
660 *in Physics Research Section A: Accelerators, Spectrometers, Detectors and Associated Equipment* **621**  
661 (2010) 222–230.
- 662 [13] F. Kaether and C. Langbrandtner, *Transit time and charge correlations of single photoelectron events*  
663 *in r7081 photomultiplier tubes*, *Journal of Instrumentation* **7** (2012) P09002.
- 664 [14] B. Lubsandorzhev, P. Pokhil, R. Vasiljev and A. Wright, *Studies of prepulses and late pulses in the 8"*  
665 *electron tubes series of photomultipliers*, *Nuclear Instruments and Methods in Physics Research*  
666 *Section A: Accelerators, Spectrometers, Detectors and Associated Equipment* **442** (2000) 452–458.
- 667 [15] K. Ma, W. Kang, J. Ahn, S. Choi, Y. Choi, M. Hwang et al., *Time and amplitude of afterpulse*  
668 *measured with a large size photomultiplier tube*, *Nuclear Instruments and Methods in Physics*  
669 *Research Section A: Accelerators, Spectrometers, Detectors and Associated Equipment* **629** (2011)  
670 93–100.

- 671 [16] S. Torre, T. Antonioli and P. Benetti, *Study of afterpulse effects in photomultipliers*, *Review of*  
672 *scientific instruments* **54** (1983) 1777–1780.
- 673 [17] M. Aartsen, K. Abraham, M. Ackermann, J. Adams, J. Aguilar, M. Ahlers et al., *Characterization of*  
674 *the atmospheric muon flux in icecube*, *Astroparticle physics* **78** (2016) 1–27.
- 675 [18] M. Aartsen, R. Abbasi, Y. Abdou, M. Ackermann, J. Adams, J. Aguilar et al., *Measurement of south*  
676 *pole ice transparency with the icecube led calibration system*, *Nuclear Instruments and Methods in*  
677 *Physics Research Section A: Accelerators, Spectrometers, Detectors and Associated Equipment* **711**  
678 (2013) 73–89.
- 679 [19] M. Aartsen, R. Abbasi, M. Ackermann, J. Adams, J. Aguilar, M. Ahlers et al., *Energy reconstruction*  
680 *methods in the icecube neutrino telescope*, *Journal of Instrumentation* **9** (2014) P03009.
- 681 [20] R. Dossi, A. Ianni, G. Ranucci and O. J. Smirnov, *Methods for precise photoelectron counting with*  
682 *photomultipliers*, *Nuclear Instruments and Methods in Physics Research Section A: Accelerators,*  
683 *Spectrometers, Detectors and Associated Equipment* **451** (2000) 623–637.
- 684 [21] M. Aartsen, K. Abraham, M. Ackermann, J. Adams, J. Aguilar, M. Ahlers et al., *Searches for sterile*  
685 *neutrinos with the icecube detector*, *Physical review letters* **117** (2016) 071801.